Check for updates

AGU ADVANCING EARTH AND SPACE SCIENCES

JAMES | Journal of Advances in Modeling Earth Systems®

RESEARCH ARTICLE
10.1029/2026MS005831

Key Points:

- Sensitive areas of mesoscale eddies exhibit distinct spatial characteristics across different latitudinal bands
- Targeted observations of mesoscale eddies across different latitudinal bands significantly improve sea surface height anomaly forecasts in these regions
- Latitude-dependent sensitive areas in mesoscale eddies arise from barotropic instability modulated by the planetary β-effect

Correspondence to:
W. Duan,
duanws@lasg.iap.ac.cn

Citation:
Jiang, L., Duan, W., & Wang, H. (2026). Latitude-dependent sensitive areas for targeted observations of mesoscale eddies associated with sea surface height anomaly forecasts. *Journal of Advances in Modeling Earth Systems*, *18*, e2026MS005831. https://doi.org/10.1029/2026MS005831

Received 19 MAR 2026
Accepted 9 JUL 2026

Author Contributions:
Conceptualization: Lin Jiang, Wansuo Duan
Data curation: Lin Jiang
Formal analysis: Lin Jiang
Funding acquisition: Lin Jiang, Hui Wang
Investigation: Lin Jiang
Methodology: Lin Jiang, Wansuo Duan
Project administration: Wansuo Duan
Software: Lin Jiang
Supervision: Wansuo Duan
Validation: Lin Jiang
Visualization: Lin Jiang
Writing – original draft: Lin Jiang
Writing – review & editing: Lin Jiang, Wansuo Duan, Hui Wang

© 2026 The Author(s). Journal of Advances in Modeling Earth Systems published by Wiley Periodicals LLC on behalf of American Geophysical Union. This is an open access article under the terms of the Creative Commons Attribution License, which permits use, distribution and reproduction in any medium, provided the original work is properly cited.

Latitude-Dependent Sensitive Areas for Targeted Observations of Mesoscale Eddies Associated With Sea Surface Height Anomaly Forecasts

Lin Jiang[1], Wansuo Duan[2,3], and Hui Wang[4]

[1]College of Oceanic and Atmospheric Sciences, Ocean University of China, Qingdao, China, [2]State Key Laboratory of Earth System Numerical Modeling and Application, Institute of Atmospheric Physics, Chinese Academy of Sciences, Beijing, China, [3]Collaborative Innovation Center on Forecast and Evaluation of Meteorological Disasters, Nanjing University of Information Science and Technology, Nanjing, China, [4]National Marine Environmental Forecasting Center, Beijing, China

Abstract By employing the conditional nonlinear optimal perturbation approach within a two-layer quasigeostrophic (QG) model, we investigate the sensitive areas for targeted observations of mesoscale eddies relevant to sea surface height anomaly (SSHA) forecasting and reveal their pronounced latitude dependence. Our results show that the spatial characteristics of sensitive areas may differ markedly among eddies located in different latitudinal bands, although these areas are generally situated in regions characterized by clear high-to low-velocity gradients, with velocity decreasing spatially along the direction of eddy rotation. For eddies at high latitudes, sensitive areas are primarily located in regions exhibiting the most pronounced high-to low-velocity gradients within the vortex. However, at low latitudes, the sensitivity is not determined solely by the magnitude of the velocity gradient; instead, the zonal velocity direction within the gradient region also plays a crucial role. Specifically, sensitive areas preferentially emerge where high-to low-velocity gradients coincide with an eastward velocity component, even when the gradients are relatively weaker. Observing system simulation experiments further confirm that prioritizing data assimilation in the identified sensitive areas within specific latitudinal regimes significantly improves SSHA forecast skill. From a dynamical perspective, the latitude-dependent sensitivity patterns can be physically interpreted in terms of barotropic instability modulated by the planetary β-effect. These findings provide practical guidance for optimizing targeted observation strategies in realistic oceanic settings, highlighting the critical role of latitude in the selection of observation sites for mesoscale eddies and ultimately enhancing SSHA forecasting capability.

Plain Language Summary Accurate representation of mesoscale eddies is important for improving ocean forecasts. Owing to their highly nonlinear nature, small initial errors in certain parts of an eddy can grow rapidly and strongly affect predictions. Observations made in these especially sensitive areas can therefore greatly improve forecast accuracy. Previous studies suggested that such sensitive areas are usually located in regions of the strongest high-to low-velocity gradients within an eddy along its rotation direction. However, our results show that this is not always the case, considering the latitudinal variation in mesoscale eddy characteristics. We find that the locations of sensitive areas also depend on latitude, with low-latitude eddies behaving differently from those at high latitudes. This means that knowing an eddy's latitude helps identify where observations will be most effective. Considering latitude can lead to more efficient observing strategies and improved forecasts of sea surface height anomaly.

1. Introduction

Oceanic mesoscale eddies are ubiquitous coherent rotating structures of water with radial scales ranging from 25 to 250 km and lifetimes spanning 10–100 days, which can be considered as an approximation to the geostrophic balance (Chelton et al., 2011). These eddies, characterized by their energetic dominance and high nonlinearity, play a crucial role in modulating the general circulation of the ocean and also contribute significantly to the mixing and transport of heat, salt, and biogeochemical tracers (Dong et al., 2014; Ni et al., 2020; Wunsch, 1999; Z. Zhang et al., 2014). Mesoscale eddies have been demonstrated to impact near-surface winds, clouds, and rainfall in their vicinity (Chelton, 2013). With such broad impacts, knowledge of mesoscale eddies holds significant implications for depicting future ocean states and related aspects of biological, chemical, and geological oceanography (Robinson, 1983), as well as for describing future atmospheric conditions (Frenger et al., 2013).

Recent advancements in satellite technology have made it possible to routinely acquire satellite observations for characterizing mesoscale eddies. Moreover, field observations are a useful complement (Z. Zhang et al., 2019). Integrating these observations into numerical models through data assimilation holds the potential to greatly refine the simulation of mesoscale eddies, enhancing the precision of initial conditions and consequently bolstering the forecasting accuracy of numerical models. However, it is important to note that the spatial and temporal sampling frequency of satellites still falls short of the requirements of increasingly developed high-resolution numerical models, particularly for real-time forecasts (Cotton & Menard, 2006). Moreover, assimilating additional observations in regions that are highly sensitive to the initial values of forecasts can significantly improve forecasting accuracy. In contrast, in areas with low sensitivity, the benefits of assimilation may be limited, and in some cases, forecasting skill could even degrade due to errors introduced by imperfect assimilation methods or unresolved model processes (Janjic et al., 2018). Therefore, even when a large volume of observations is available, it remains essential to prioritize assimilation in regions where it is most critical to achieve optimal forecasting performance. To address these embarrassments, and drawing on the crucial role that mesoscale eddies play in the ocean, research is increasingly focused on optimizing the use of limited observations to effectively describe mesoscale eddies, thereby enhancing forecasting skills for ocean state.

Through observing system simulation experiments, Weiss and Grooms (2017) suggested that precise initialization of mesoscale eddies improves sea surface height (SSH) forecasting accuracy. Specifically, they found that assimilating evenly distributed nine-point observations of eddies is the most effective strategy for this purpose. Nevertheless, it's crucial to emphasize that mesoscale eddies exhibit irregular shapes and asymmetric flow fields, characterized by highly nonlinear features (Chelton et al., 2011; Tang et al., 2020). In light of this, the uniform assimilation strategy may not adequately capture the nonlinear characteristics of eddies, and, therefore, may not necessarily maximize SSH forecasting skill. Jiang et al. (2022) proposed that there should be certain key regions on mesoscale eddies where prioritizing additional observations with specific distribution characteristics can more effectively improve SSH forecasting skill. This idea aligns with the observational strategy entitled "target observation" (Mu, 2013; Snyder, 1996), which aims to improve the prediction of an event at a future time t_1 (the verification time) within predefined areas of interest (verification areas) by strategically deploying additional observations at a specific time t_2 (the targeted time; typically $t_2 < t_1$) in key areas (sensitive areas). These additional observations in sensitive areas are expected to exert a considerable influence on forecasts within the verification area. By giving precedence to assimilating targeted observations in sensitive areas, more reliable initial conditions can be established, thereby enhancing the accuracy of predictions for pertinent events more effectively.

At present, a series of encouraging results have been achieved in theoretical research and related field experiments of target observations for high-impact weather and climate event forecasting. For instance, the Observing System Research and Predictability Experiment (THORPEX), organized by the World Meteorological Organization during 2005–2014, employed singular vector and Ensemble Transform Kalman Filter methods to identify sensitive areas and demonstrated the important role of targeted observations in improving tropical cyclone track forecasts (Gelaro et al., 2010). Moreover, the Dropwindsonde Observation for Typhoon Surveillance near the Taiwan Region (DOTSTAR) program has employed the adjoint-derived sensitivity steering vector method to guide aircraft observations since 2003, significantly improving operational typhoon forecasting in Taiwan (Wu et al., 2007, 2009). Compared with atmospheric applications, oceanic target observation studies have developed more recently. Representative examples include the identification of sensitive areas for Kuroshio large meander prediction using singular vector analysis (Fujii et al., 2008) and the determination of optimal observation locations for decadal predictions of Kuroshio Extension path transitions using particle filter techniques (Kramer et al., 2012). However, it should be noted that most of the above studies and field experiments, whether in the atmosphere or the ocean, have relied to varying degrees on linear approximations when identifying sensitive areas. As a result, the effects of nonlinear physical processes may be underestimated, potentially leading to discrepancies between the identified sensitive areas and the actual optimal observation areas. To overcome this limitation, Mu et al. (2009) introduced the Conditional Nonlinear Optimal Perturbation (CNOP) method (Mu et al., 2003) into target observation studies. Unlike traditional linear approaches, CNOP fully accounts for the nonlinear evolution of initial perturbations and thus provides a more realistic framework for identifying sensitive areas (Mu et al., 2009). Since then, the CNOP method has been successfully applied to a variety of high-impact atmosphere-ocean phenomena, including tropical cyclones, heavy rainfall, dust storm events, PM2.5 forecasts, the Kuroshio, circulation systems in the South China Sea, the El Niño-Southern Oscillation, and the Indian Ocean

19422466, 2026, 8, Downloaded from https://agupubs.onlinelibrary.wiley.com/doi/10.1029/2026MS005831 by CochraneChina, Wiley Online Library on [31/07/2026]. See the Terms and Conditions (https://onlinelibrary.wiley.com/terms-and-conditions) on Wiley Online Library for rules of use; OA articles are governed by the applicable Creative Commons License

Dipole (Chan et al., 2023; Duan et al., 2018; R. Feng & Duan, 2025; J. Feng et al., 2023; Li et al., 2014; Liang et al., 2019; Liu et al., 2021; Qin et al., 2022; Q. Wang et al., 2013; L. Yang & Duan, 2024; L. Yang et al., 2022, 2023; K. Zhang et al., 2019).

Jiang et al. (2022) applied the CNOP method to investigate sensitive areas for targeted observations of mesoscale eddies in a quasigeostrophic (QG) model for SSH anomaly (SSHA) forecasts, indicating where observations should be preferentially deployed to better match the structure and irregular characteristics of the eddies. Specifically, they found that the sensitive areas for mesoscale eddies in SSHA forecasting are located in regions where the eddies present the most pronounced high-to low-velocity gradients along their rotation. By using multiple sets of realistic oceanic data, Jiang et al. (2023) demonstrated that preferentially assimilating additional observations into such sensitive areas within mesoscale eddies in the Kuroshio Extension region can significantly enhance SSHA forecasting skill, which confirms the validity of the sensitive areas identified in Jiang et al. (2022). Moreover, Jiang et al. (2024) used the CNOP approach in the QG model to explore the target observation of paired mesoscale eddies. They revealed that, in addition to the sensitive areas on the eddies themselves, there are also sensitive areas for SSHA forecasting between co-rotating eddies, which emphasizes the impact of interactions between eddies on the sensitive areas for SSHA forecasting and deepens the understanding of the crucial role that accurately describing mesoscale eddies plays in improving SSHA forecasting skills.

The aforementioned studies provide valuable guidance for the initialization of mesoscale eddies, which is a crucial step toward improving SSHA forecast accuracy. However, it should be noted that the investigations by Jiang et al. (2022, 2024) were conducted under the f-plane approximation, without adequately accounting for latitude information. In reality, mesoscale eddies are ubiquitous throughout the global ocean and exhibit a nonuniform distribution, being abundant in subtropical to mid-latitude regions and relatively sparse near the equator and in polar areas. Moreover, mesoscale eddies display pronounced differences in their characteristics across different latitudinal bands, including variations in horizontal scale, drift speed, and other properties. These facts naturally raise the question of whether the characteristics of sensitive areas remain invariant across different latitudinal bands despite the strong latitude dependence of eddy properties. Jiang et al. (2023) demonstrated that the sensitive areas identified in Jiang et al. (2022) are applicable to the Kuroshio Extension region; however, it remains unclear whether these sensitive areas are similarly valid across other latitudinal bands, particularly in the subtropical band where mesoscale eddies are statistically prevalent. Collectively, these considerations motivate a practical question: is it necessary to explicitly consider the latitude of mesoscale eddies when designing and deploying targeted observation strategies?

To address the above question, the present study investigates the sensitive areas of mesoscale eddies associated with SSHA forecasting while explicitly accounting for their latitudinal locations. The ultimate objective is to consider more realistic oceanic scenarios and to provide robust and practical guidance for field campaigns involving targeted observations of mesoscale eddies. In ocean numerical models, latitudinal information is primarily represented through the Coriolis parameter and its meridional gradient (the planetary β-effect). To facilitate comparison with previous studies, we employ a QG model similar to those used by Jiang et al. (2022) and Weiss and Grooms (2017), with the key distinction that the Coriolis parameter and its meridional gradient are explicitly included in this study.

The organization of this paper is as follows. In Section 2, we briefly introduce the QG model and the CNOP approach. In Section 3, CNOP-type initial errors of mesoscale eddies are calculated, with particular attention paid to eddies at low, mid, and high latitudes, and the corresponding sensitive areas are subsequently identified. Section 4 describes the design of observing system simulation experiments to verify the sensitive areas of mesoscale eddies at specific latitudes and to assess their effectiveness in improving SSHA forecast skill. In Section 5, the latitude-dependent sensitivity patterns are physically interpreted from the perspective of barotropic instability associated with the planetary β-effect. Finally, Section 6 presents a summary and discussion.

2. Model and Methodology

2.1. The Two-Layer Quasigeostrophic Model

The doubly periodic quasigeostrophic (QG) model with two equal layers on a β-plane is adopted. The model is subject to a vertically sheared zonal flow that is horizontally uniform and baroclinically unstable. Through

19422466, 2026, 8, Downloaded from https://agupubs.onlinelibrary.wiley.com/doi/10.1029/2026MS005831 by CochraneChina, Wiley Online Library on [31/07/2026]. See the Terms and Conditions (https://onlinelibrary.wiley.com/terms-and-conditions) on Wiley Online Library for rules of use; OA articles are governed by the applicable Creative Commons License

decomposition of the instantaneous field into mean and perturbation fields, the governing equations for perturbation evolution derived from the two-layer QG model can be expressed as follows.

$$\partial_t q_1 = -\mathbf{U}_1 \cdot \nabla q_1 - \partial_x q_1 - (k_b + 1)\, v_1 - \nu \nabla^8 q_1 \tag{1}$$

$$\partial_t q_2 = -\mathbf{U}_2 \cdot \nabla q_2 + \partial_x q_2 - (k_b - 1)\, v_2 - c_d \cdot \nabla \times (|\mathbf{U}_2|\mathbf{U}_2) - \nu \nabla^8 q_2 \tag{2}$$

$$q_1 = \nabla^2 \psi_1 + \frac{1}{2}(\psi_2 - \psi_1) \tag{3}$$

$$q_2 = \nabla^2 \psi_2 - \frac{1}{2}(\psi_2 - \psi_1) \tag{4}$$

Equations 1–4 have been nondimensionalized using the deformation radius as a length scale and the imposed zonal velocity as a velocity scale. q_i represents the potential vorticity and ψ_i represents the streamfunction ($i = 1$, 2, corresponding to the first and second layer of the model), $\mathbf{U}_i$ is the two-dimensional vector composed of zonal velocity $u_i = -\partial_y \partial \psi_i$ and meridional velocity $v_i = \partial_x \partial \psi_i$, $c_d (=0.1)$ is the standard quadratic drag coefficient and $\nu \left(=5 \times 10^{-7}\right)$ is the hyperviscosity coefficient. Note that the Coriolis parameter f is implicitly included in the nondimensional equations; k_b serves as a numerical parameter representing the intensity of the planetary β-effect. The model domain is square, with a nondimensional width of 32 π. Computational solutions for this model are obtained using 256 × 256 nonzero Fourier modes and a fourth-order semi-implicit Runge-Kutta scheme (Weiss & Grooms, 2017). The nondimensional grid size is 0.39, providing more than two grid points per deformation radius, which is adequate for eddy-resolving simulations. The nondimensional time step is 0.01.

In Weiss and Grooms (2017), mesoscale eddies were identified in a simulation conducted on an f-plane. The averaged vortex exhibited a radius of 5 grid points and a maximum nondimensional velocity of 18. By assigning a dimensional value of 15 km to the spatial grid (corresponding to a dimensional deformation radius of 38.2 km) and 1 cm/s to the velocity, they obtained vortex statistics that closely matched the properties of real-world mesoscale eddies. In contrast, the present study explicitly accounts for specific latitudinal information and incorporates the planetary β-effect, under which the dimensional deformation radius varies with latitude. To better relate the nondimensional QG model to real-world conditions, we retain a dimensional velocity scale of 1 cm/s and use the statistical deformation radius in reality to define the model length scale at the corresponding latitude. The zonal-mean deformation radius generally decreases with increasing latitude (Chelton et al., 2011), implying that the corresponding dimensional grid spacing in the QG model also varies with latitude. Notably, the value of k_b in the nondimensional model depends on both the characteristic velocity and length scales. For instance, at 30° latitude, the statistical zonal-mean deformation radius is approximately 40 km (Chelton et al., 2011), which corresponds to a grid spacing of 15.708 km in the model. Under this scaling, the dimensional meridional gradient of the Coriolis parameter in reality ($\beta \approx 1.98 \times 10^{-11} \mathrm{m}^{-1} \mathrm{s}^{-1}$) is mapped to a specific nondimensional $k_b = 3.168$. At 60° latitude, where the deformation radius decreases to approximately 10 km, the corresponding grid spacing becomes 3.927 km, resulting in a different nondimensional $k_b = 0.114$ in the QG model. The corresponding vortex statistics derived from the model are presented in Section 3.

2.2. CNOP

To comprehensively consider the nonlinearity of mesoscale eddies, the CNOP method, a nonlinear technique of target observation, is adopted in this paper. The CNOP, as defined by Mu et al. (2003), represents the initial perturbation that adheres to a particular physical constraint and exhibits the most significant nonlinear evolution at a specified prediction time. In this subsection, we will offer a brief overview of the CNOP. More details can be seen in Mu et al. (2003).

In this study, the streamfunction of the first layer ψ_1 in the QG model is used to represent SSHA, which is subsequently perturbed and forecast. Mathematically, the CNOP is obtained by solving an optimization problem with respect to the initial perturbations. The cost function for the problem considered here can be expressed as

$$J\left(\psi_{1,0}^{*}\right) = \max_{\psi'_{1,0} \in C_\delta} J\left(\psi'_{1,0}\right), J\left(\psi'_{1,0}\right) = \|M_t\left(\psi_{1,0} + \psi'_{1,0}\right) - M_t\left(\psi_{1,0}\right)\|_A \tag{5}$$

19422466, 2026, 8, Downloaded from https://agupubs.onlinelibrary.wiley.com/doi/10.1029/2026MS005831 by CochraneChina, Wiley Online Library on [31/07/2026]. See the Terms and Conditions (https://onlinelibrary.wiley.com/terms-and-conditions) on Wiley Online Library for rules of use; OA articles are governed by the applicable Creative Commons License

where M_t represents the forward integration (a forecast) of the model with its initial condition. $M_t(\psi_{1,0})$ and $M_t(\psi_{1,0} + \psi'_{1,0})$ denote two forecasts generated by the same model but with distinct initial conditions $\psi_{1,0}$ and $\psi_{1,0} + \psi'_{1,0}$, respectively. The disparity lies in the fact that an initial perturbation $\psi'_{1,0}$ is added to the original initial conditions $\psi_{1,0}$. J represents one cost function evaluating the nonlinear evolution of the initial perturbation $\psi'_{1,0}$ at prediction time t and δ constrains the scope of the initial perturbations. Here, L2 norm is used as $\|\cdot\|_A$ to measure the evolution of perturbation. In addition, Equation 6 is employed to constrain the amplitude of initial perturbations:

$$\delta = \left\{ \psi'_{1,0} \middle| \sqrt{\frac{1}{n}\sum_{i=1}^{n}\left(\psi'_{1,0}\right)_i^2} \leq \tau \cdot \left(\psi_{1,0}\right)_{\mathrm{STD}} \right\} \tag{6}$$

where n is the number of perturbed grids, τ is a predefined positive number, $\left(\psi_{1,0}\right)_{\mathrm{STD}}$ denotes the standard deviation of the $\psi_{1,0}$ across the entire model domain. Specifically, τ is set to 0.06 to ensure that the initial perturbations of SSHA at each grid point remain within the typical observational errors of 0.01–0.03 m.

The resulting initial perturbation $\psi^*_{1,0}$ is precisely the CNOP and is calculated using the Spectral Projected Gradient 2 (SPG2) algorithm (Birgin et al., 1999). Note that the gradient of the objective function J with respect to the initial value, representing the fastest descending direction of the cost function and playing a crucial role in the SPG2 algorithm, is computed using the numerical derivative method here.

3. The Most Sensitive Initial Error of Mesoscale Eddies Associated With SSHA Forecasting at Different Latitudes

As introduced above, CNOPs represent the most sensitive initial perturbations in a nonlinear model and have been shown to be particularly effective in identifying areas of high sensitivity for targeted observations. CNOPs typically manifest in areas with notably heightened perturbation energies, and the accuracy of forecasts is notably sensitive to initial errors within these areas. Hence, these areas can be regarded as critical sensitive areas for targeting observation. In this section, we investigate the CNOPs of mesoscale eddies in the context of SSHA forecasting at several representative latitudes and identify the sensitive areas that warrant particular attention for targeted observations.

It is essential to note, as mentioned in the introduction, that latitudinal variations in ocean dynamics are primarily represented through the latitude dependence of the Coriolis parameter and its meridional gradient (i.e., the planetary β-effect). Here, we investigate CNOPs under several prescribed values of the nondimensional parameter k_b in the QG model, which represents the planetary β-effect, with each value corresponding to a specific latitude regime (see Section 2.1). By conducting CNOP calculations for multiple k_b settings, we aim to facilitate systematic comparisons and to gain deeper insight into the sensitivity characteristics of mesoscale eddies at different latitudes. Specifically, based on the derivation in Section 2.1, in high-latitude regions ($\theta > 60°$, θ signifies the latitude), $k_b < 0.114$; in mid-latitude regions ($30° < \theta < 60°$), $0.114 < k_b < 3.168$; and in low-latitude regions ($\theta < 30°$), $k_b > 3.168$. Accordingly, six values of k_b (0, 0.1, 1, 2, 5 and 10) are considered in this section, corresponding to nondimensional estimates derived from realistic planetary β parameters. Note that $k_b = 0$ corresponds to the f-plane approximation and may be regarded as an idealized extreme high-latitude condition. A value of $k_b = 0.1$ represents high-latitude conditions, $k_b = 1$ or $k_b = 2$ corresponds to mid-latitude conditions, and $k_b = 5$ or $k_b = 10$ characterizes low-latitude conditions.

Before calculating the CNOPs, we first integrated the QG model to time T_0 with $k_b = 0$ to obtain a flow field rich in mesoscale eddies. The integration was initialized from a (ψ_1, ψ_2) matrix composed of random numbers drawn from a normal distribution $N(0, 1)$. Using this eddy-rich flow field at time T_0 as the initial condition, mesoscale eddies were identified with a simplified SSHA-based identification method (Weiss & Grooms, 2017), and CNOP calculations were subsequently performed under multiple k_b settings. This experimental design ensures that CNOP fields are computed for identical initial vortices while only varying k_b, thereby effectively controlling other factors and enabling a direct comparison across different latitude regimes. Notably, the mean nondimensional eddy radius at time T_0 was approximately 5 grid points. According to the spatial grid configuration in Section 2.1, this corresponds to a dimensional radius of approximately 78.5 km at 30°latitude and 19.6 km at 60° latitude.

19422466, 2026, 8, Downloaded from https://agupubs.onlinelibrary.wiley.com/doi/10.1029/2026MS005831 by CochraneChina, Wiley Online Library on [31/07/2026]. See the Terms and Conditions (https://onlinelibrary.wiley.com/terms-and-conditions) on Wiley Online Library for rules of use; OA articles are governed by the applicable Creative Commons License

Specifically, for $k_b = 10$, which corresponds to about 15°latitude, the nondimensional eddy radius translates to a dimensional radius of about 128 km, given that the corresponding deformation radius is approximately 65 km. In addition, we also compiled statistics of the mean eddy radius at time T_1, which are largely consistent with those at T_0. Overall, the dimensional mean eddy radius in the model decreases with increasing latitude and is consistent with the characteristic spatial scales of real mesoscale eddies, ranging from tens to several hundred kilometers. Furthermore, starting from the initial condition at T_0, the model was independently integrated under six k_b settings (0, 0.1, 1, 2, 5, and 10) to examine eddy propagation speeds under different dynamical conditions. The results indicate that, for the same eddy identified at T_0, the propagation speed increases with increasing k_b. Using a dimensional velocity scale of 1 cm/s, the majority of identified eddies exhibited propagation speeds below 25 cm/s, consistent with realistic oceanic observations. Only a few isolated cases display markedly higher propagation speeds under $k_b = 5$ and 10, occasionally exceeding 50 cm/s. Although mesoscale eddies are known to propagate relatively fast at low latitudes, these exceptionally fast-moving features, despite having spatial scales comparable to those of mesoscale eddies, propagate at speeds that substantially exceed those expected for freely propagating mesoscale eddies governed by the β-effect. Such features are therefore more appropriately interpreted as eddy-like structures or eddy-wave hybrid features, rather than classical mesoscale eddies. To ensure a conservative and robust selection, only vortices with dimensional propagation speeds below 25 cm/s are classified as mesoscale eddies and retained for the experiments in this study.

For the identified mesoscale eddies, six sets of CNOP experiments were conducted for each, corresponding to the six prescribed values of k_b listed above. Specifically, in each experiment, the streamfunction (ψ_1, ψ_2) at time T_0 was taken as the initial condition, and the model was integrated forward to time T_1 ($T_1 > T_0$) using the prescribed k_b value. The resulting evolution of SSHA from T_0 to T_1 was regarded as the reference state for prediction. The time interval between T_0 and T_1 was set to 1 week (i.e., 7 days), consistent with Jiang et al. (2022), corresponding to the 350th week of the model integration. The SSHA perturbation was imposed on the identified initial eddy, and the SSHA forecast was defined within a rectangular domain encompassing the identified initial eddy and its subsequent position after the 7-day evolution. Based on the CNOP framework, the most sensitive initial perturbations of SSHA forecasts with a lead time of 7 days were then obtained under each prescribed k_b setting of the QG model. In total, these CNOP experiments were performed for 25 predetermined eddies in the initial field, yielding 150 CNOP error patterns.

Analysis of the experimental results shows that the locations of dominant CNOP errors within a vortex may vary with the value of k_b, while generally remaining confined to regions characterized by high-to low-velocity gradients along the eddy rotation, especially for eddies containing more than one such gradient region. To be more specific, when such eddies are located at high latitudes, corresponding to experiments conducted with $k_b = 0$ or 0.1, the CNOPs tend to concentrate in the region with the most pronounced high-to low-velocity gradient within the eddy and display a shear structure, in agreement with the results of Jiang et al. (2022). However, for eddies at low latitudes, corresponding to experiments with $k_b = 5$ or 10, CNOPs are increasingly likely to occur in regions where high-to low-velocity gradients coincide with an eastward velocity component, even if the gradient itself is relatively weak. This result suggests that, under low-latitude conditions, the zonal velocity direction within the high-to low-velocity gradient region becomes an additional key factor in determining the locations of large CNOPs, rather than the magnitude of the velocity gradient alone. For eddies at mid latitudes, large CNOP values may occur in both types of regions. A representative example is shown in Figure 1, where the eddy contains two regions of high-to low-velocity gradients. When $k_b = 0$ or $k_b = 0.1$, the CNOPs predominantly occur in area "A," which is characterized by a stronger high-to low-velocity gradient. When $k_b = 1$ or $k_b = 2$, corresponding to "mid-latitude" conditions, the CNOPs appear not only in area "A" but also in area "B." Although area "B" exhibits a relatively weaker velocity gradient, it features an eastward velocity component ($u > 0$). When $k_b = 5$ or $k_b = 10$, representing low-latitude conditions, the CNOPs primarily concentrate in area "B" rather than area "A." By comparison, for eddies characterized by a single high-to low-velocity gradient region, as illustrated in Figure 2, the calculated CNOPs consistently concentrate within that gradient region and exhibit a shear structure, regardless of the k_b setting used in the experiments.

The regions exhibiting significant perturbation energies within the CNOP patterns indicate the sensitive areas for target observation. The analyses above reveal that the spatial characteristics of the sensitive areas may differ among eddies located in different latitudinal bands, although these areas are generally situated in regions characterized by clear velocity gradients along the eddy's rotational direction. For eddies at high latitudes, the sensitive

19422466, 2026, 8, Downloaded from https://agupubs.onlinelibrary.wiley.com/doi/10.1029/2026MS005831 by CochraneChina, Wiley Online Library on [31/07/2026]. See the Terms and Conditions (https://onlinelibrary.wiley.com/terms-and-conditions) on Wiley Online Library for rules of use; OA articles are governed by the applicable Creative Commons License

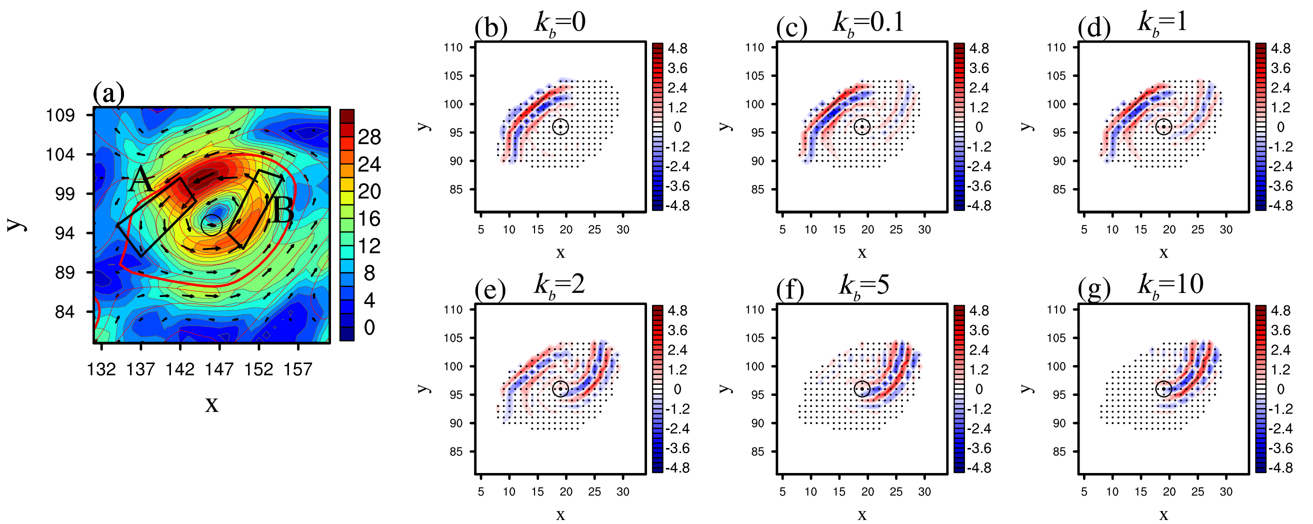

Figure 1. A representative eddy featuring two high-to low-velocity gradient regions, as illustrated by the initial velocity field in (a) (shaded). Panels (b–g) show the corresponding conditional nonlinear optimal perturbation fields (shaded) calculated under different values of k_b, namely 0, 0.1, 1, 2, 5, and 10, respectively. Black "⊙" marks the initial centers of eddies, and black arrows represent the velocity vectors. Red contours depict the initial sea surface height anomaly field, with bold contours delineating the vortex edges. The black quadrilaterals in (a) mark the regions where high-to low-velocity gradients are observed. Taking the CNOPs in (b) and (f) as examples, their evolution during the optimization period is shown in Figure 3.

areas determined by CNOPs are confined to regions with the strongest high-to low-velocity gradients along the eddy rotation. In contrast, for low-latitude eddies, sensitive areas are increasingly likely to occur in regions where a (relatively weaker) high-to low-velocity gradient coincides with an eastward velocity component. In this context, it is essential to highlight that, beyond the presence of a high-to low-velocity gradient, the eastward velocity component (u > 0) within such a gradient region becomes a key criterion for identifying the most sensitive area for SSHA forecasting, especially for low-latitude mesoscale eddies featuring more than one velocity gradient region. As for mid-latitude eddies, sensitive areas of both types may be important for targeted observation.

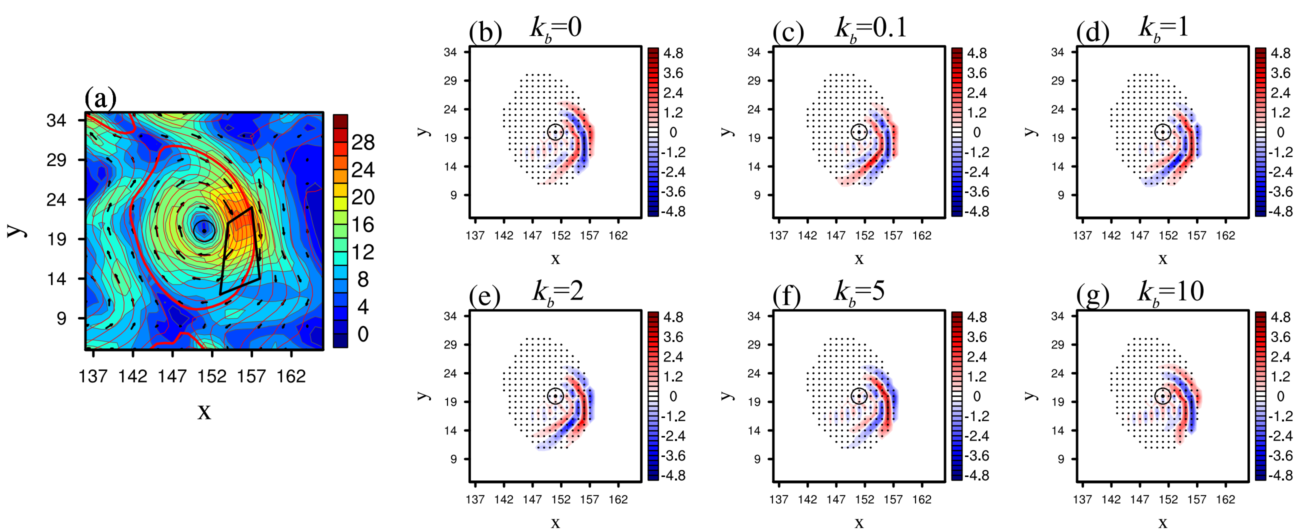

Figure 2. A representative eddy featuring a single high-to low-velocity gradient region, as illustrated by the initial velocity field in (a) (shaded). Panels (b–g) show the corresponding conditional nonlinear optimal perturbation fields (shaded) calculated under different values of k_b, namely 0, 0.1, 1, 2, 5, and 10, respectively. Black "⊙" marks the initial centers of eddies, and black arrows represent the velocity vectors. Red contours depict the initial sea surface height anomaly field, with bold contours delineating the vortex edges. The black quadrilateral in panel (a) marks the region where high-to low-velocity gradient is observed.

19422466, 2026, 8, Downloaded from https://agupubs.onlinelibrary.wiley.com/doi/10.1029/2026MS005831 by CochraneChina, Wiley Online Library on [31/07/2026]. See the Terms and Conditions (https://onlinelibrary.wiley.com/terms-and-conditions) on Wiley Online Library for rules of use; OA articles are governed by the applicable Creative Commons License

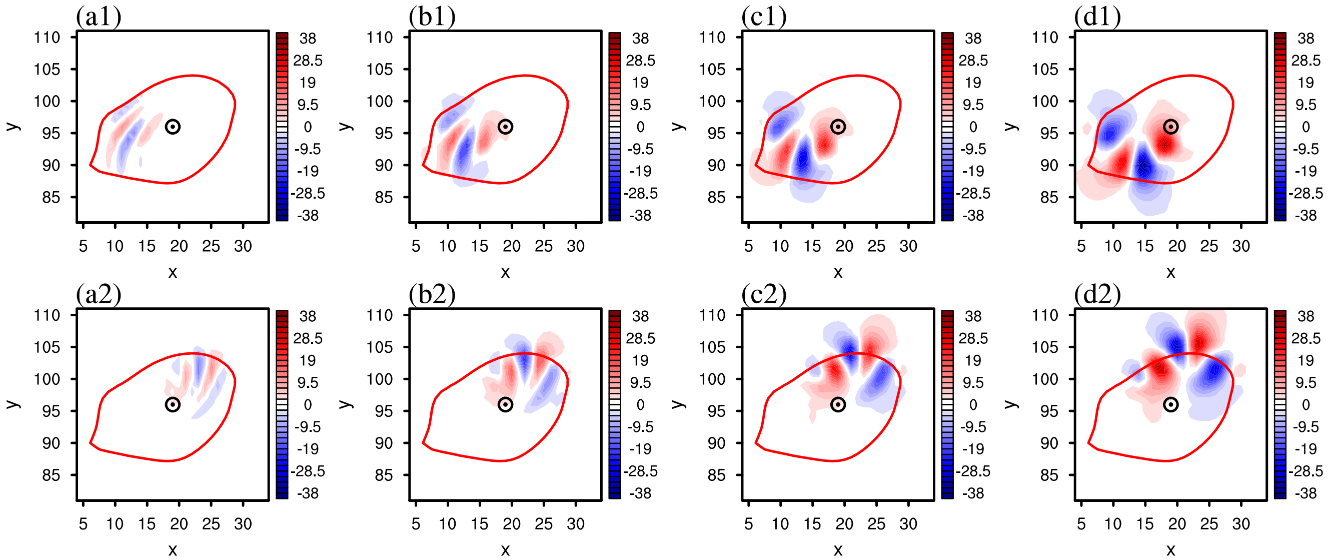

Figure 3. CNOP-triggered forecast errors (shaded) for the eddy shown in Figure 1a are plotted in (a) at time $(1/4)\,(T_1 - T_0)$, (b) at time (1/2) $(T_1 - T_0)$, (c) at time (3/4) $(T_1 - T_0)$, and (d) at time T_1, where $[T_0, T_1]$ denotes the optimization period. (1, 2) correspond to the scenarios with $k_b = 0$ and $k_b = 5$, respectively. The red contours indicate the edge of the initial eddy, and the black "⊙" marks the center of the initial eddy.

Note that among the 25 predetermined eddies, 16 exhibit behavior consistent with that shown in Figure 1, while the other five are consistent with Figure 2. Among the remaining four eddies, although multiple high-to low-velocity gradient regions exist within the eddy, a sufficiently large disparity in gradient strength causes the CNOPs to remain concentrated within the strongest gradient region regardless of the setting of k_b. This suggests that, while the presence of an eastward velocity component within a gradient region is a key criterion for determining the most sensitive areas of mesoscale eddies in SSHA forecasting, it is not a decisive factor. When the strongest high-to low-velocity gradient region within an eddy is overwhelmingly dominant, the sensitive area may still remain within that region regardless of where the vortex is located.

In summary, the CNOP experiments reveal potential differences in the spatial characteristics of sensitive areas for mesoscale eddies at high, middle and low latitudinal bands. These results highlight that the sensitive areas identified by Jiang et al. (2022) are not universally applicable to all eddies. When conducting targeted observations of mesoscale eddies, the optimal deployment of observational assets may also need to consider the eddy's latitudinal position. Notably, we identified a type of sensitive area characterized by relatively weak high-to low-velocity gradients coexisting with eastward velocity components within the vortex, particularly for eddies at mid and low latitudes. This type of sensitive area has not been reported in previous studies. Furthermore, we tested an optimization period of 10 days and found that the experimental results were almost unaffected, which strengthens the robustness of the above conclusions. Then, what is the feasibility of using such sensitive areas for targeted SSHA observations, especially at different latitudes? This issue will be addressed through numerical experiments in the next section.

4. Observing System Simulation Experiments to Assess the Effectiveness of Latitudinally Dependent Sensitive Areas

The objective of target observation is to provide the most valuable additional observations to refine the precision of the initial conditions in the numerical model, thereby significantly enhancing the forecasting accuracy of concern. The numerical validation of the target observation is confirmed when the improvement gained from assimilating additional observations in sensitive areas significantly exceeds that in other regions. Therefore, in this section, we conducted observing system simulation experiments (OSSEs; Hoffman & Atlas, 2016) to evaluate the effectiveness of the sensitive areas at different latitudinal bands in SSHA forecasting. Below, we use the vortex shown in Figure 1, which illustrates different sensitive areas under varying k_b values and reveals a type of sensitive area not identified in previous studies, to conduct the OSSEs and analyze the results. For clarity, area

19422466, 2026, 8, Downloaded from https://agupubs.onlinelibrary.wiley.com/doi/10.1029/2026MS005831 by CochraneChina, Wiley Online Library on [31/07/2026]. See the Terms and Conditions (https://onlinelibrary.wiley.com/terms-and-conditions) on Wiley Online Library for rules of use; OA articles are governed by the applicable Creative Commons License

"A" in Figure 1, identified as the sensitive area when $k_b = 0$ or 0.1, is hereafter referred to as the "f-sensitive area." The area "B," identified as the sensitive area when $k_b = 5$ or 10, is referred to as the "β-sensitive area."

Considering the six distinct k_b (0, 0.1, 1, 2, 5, 10) values outlined in the previous section, each corresponding to a specific latitude, we designed six corresponding sets of OSSEs in this section. These experiments were systematically conducted under the respective k_b settings within the QG model framework. To illustrate the experimental design, we focus on the OSSE conducted with the $k_b = 0$ as a representative example and provide a detailed description of its setup and procedures. First, the QG model was integrated from T_0 to T_1 with the $k_b = 0$, and the resulting reference state during this period was taken as the "true state," that is, the "Nature Run." Synthetic observations were then generated by adding small errors to the Nature Run at specified observation points. Next, we overlaid white noise with large amplitudes onto the Nature Run at time T_0, followed by smoothing this field using the Lanczos filtering. Utilizing the smoothed field as the initial condition, we integrated the model with the k_b setting to 0 until time T_1, producing the "Control Run," which serves as the control forecast for the Nature Run. To obtain reliable and robust results, 100 Control Runs were generated randomly here. Following that, we assimilated synthetic observations into the initial fields of the Control Runs, resulting in the revised initial fields. With the updated initial conditions, we proceeded to re-integrate the model with the k_b setting to 0 until time T_1 to produce new SSHA forecasts, referred to as the "Assimilation Runs." In these Assimilation Runs, the assimilation strategies were specifically designed for the β-sensitive area and f-sensitive area, respectively. In each sensitive area, 2-, 3-, and 4-point observations were randomly deployed and assimilated, and 40 sets of each observation configuration were generated to further ensure reliability. Optimal interpolation (see Appendix D in Jiang et al. (2022)) was then employed to assimilate the observations.

The five additional sets of OSSEs were conducted following the same procedures as the one described above for $k_b = 0$, with the only difference being the specific k_b values used, which were successively set to 0.1, 1, 2, 5, and 10. To quantify the improvement in the forecast after assimilation, we define the benefit b as follows:

$$b = [(dF_1 - dF_2)/dF_1] \times 100\% \tag{7}$$

where dF_1 and dF_2 respectively denote the forecast errors of the Control Run and the Assimilation Run relative to the Nature Run.

Then, we calculated the benefits b of assimilation within the β-sensitive area and f-sensitive area for different OSSEs, as depicted in Figure 4. The results demonstrated that, irrespective of whether 2-point, 3-point, or 4-point assimilation strategies are employed, as the value of k_b increases, the assimilation benefits b in the f-sensitive area gradually decrease. In contrast, the benefits b in the β-sensitive area increase, although they begin to decline once k_b exceeds 5. Specifically, when k_b is small, especially $k_b = 0$ or $k_b = 0.1$, signifying a scenario like the f-plane approximation or high-latitude regions, the benefits b obtained from assimilating observations within the f-sensitive area surpass those from the β-sensitive area. However, when $k_b = 5$ or $k_b = 10$, corresponding to low latitudes, the benefits b gained from assimilating observations in the β-sensitive area clearly outperforms those in the f-sensitive area. Note that at specific locations in the mid latitudes, the benefits b derived from both sensitive areas converge and become consistent.

Based on the above analysis, the OSSE results indicate that, from high to low latitudes, the effectiveness of the f-sensitive area associated with mesoscale eddies gradually weakens, while the advantages of the β-sensitive area become increasingly pronounced. When an eddy is located at high latitudes, assimilating observations within the f-sensitive area significantly enhances SSHA forecasting. In contrast, when the eddy is situated in low-latitude regions, it is increasingly likely that prioritizing the assimilation of observations within the β-sensitive area would be more effective. In mid-latitude regions, assimilating observations in both the f-sensitive area and β-sensitive area may be essential for improving SSHA forecasting skill. Similar OSSEs conducted for other eddies yield consistent results, further confirming the latitude dependence of the sensitive areas associated with mesoscale eddies. These findings underscore the effectiveness of the β-sensitive area in mid- and low-latitude regions, which has not been identified previously. Overall, these results provide valuable guidance for the optimal allocation of target observation, highlighting the critical role of latitude in selecting targeted observation sites for mesoscale eddies and thereby enabling more efficient improvements in SSHA forecasting.

19422466, 2026, 8, Downloaded from https://agupubs.onlinelibrary.wiley.com/doi/10.1029/2026MS005831 by CochraneChina, Wiley Online Library on [31/07/2026]. See the Terms and Conditions (https://onlinelibrary.wiley.com/terms-and-conditions) on Wiley Online Library for rules of use; OA articles are governed by the applicable Creative Commons License

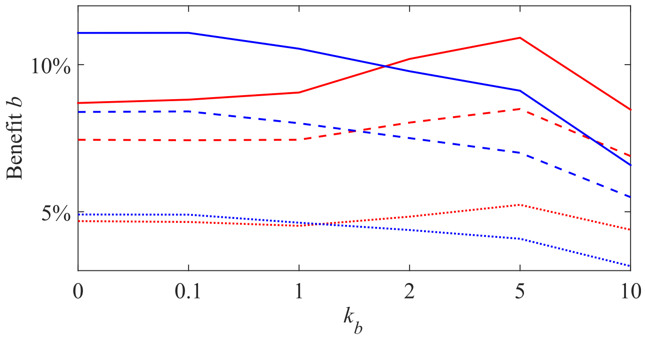

Figure 4. The mean benefits b obtained from assimilating 40 sets of 2-, 3-, and 4-grid observations in the β-sensitive and f-sensitive areas across 100 control forecasts. Red lines denote results obtained by assimilating observations in the β-sensitive area, while blue lines denote those obtained in the f-sensitive area. Dotted, dashed, and solid lines represent assimilations using two-, three-, and four-point observations, respectively.

Furthermore, how can the latitude dependence of mesoscale eddy sensitive areas be explained from a theoretical perspective? This question is addressed in the next section.

5. Interpretation

In this section, we further explain the latitude dependence of the sensitive areas in SSHA forecasting, with particular emphasis on the emergence of β-sensitive area at lower latitudes, which has not been identified previously. Indeed, the sensitive areas are identified based on the significant value of the calculated CNOPs, so the central question revolves around comprehending why the calculated CNOPs may vary with different k_b value. Now, we take the vortex shown in Figure 1 as an example, focusing on the case with $k_b = 5$ (low-latitude) and comparing it with the $k_b = 0$ case (extreme high-latitude) to gain insight into this issue. To elucidate the underlying mechanism, we employ an eddy-energy analysis following Tsujino et al. (2006).

The calculation of eddy energies typically involves decomposing an instantaneous flow into mean flow and eddy fluctuation components. The mean flow is usually obtained from the time-average of the instantaneous field, and eddy fluctuation is delineated as the instantaneous field minus the mean field. Regarding horizontal flow, it is widely recognized that the evolution of eddy fluctuation is predominantly driven by the barotropic instability of the mean flow, which fosters the transfer of kinetic energy to support the amplification of eddy fluctuations. To measure the transfer of kinetic energy from the mean flow to the eddy fluctuation triggered by barotropic instability, the barotropic conversion rate (BT) is deduced from the tendency equation of eddy kinetic energy (EKE) under the quasigeostrophic assumption.

$$\frac{\partial \mathrm{EKE}}{\partial t} = -\rho_0\left(u'u'\frac{\partial \overline{u}}{\partial x} + u'v'\left(\frac{\partial \overline{u}}{\partial y} + \frac{\partial \overline{v}}{\partial x}\right) + v'v'\frac{\partial \overline{v}}{\partial y}\right) + \text{residue}, \tag{8}$$

where $\overline{u}$ and u' represent the zonal velocities of the mean flow and the eddy fluctuation field, $\overline{v}$ and v' denote the meridional velocities of the mean flow and the eddy fluctuation field, respectively; and

$$\mathrm{BT} = -\rho_0\left(u'u'\frac{\partial \overline{u}}{\partial x} + u'v'\left(\frac{\partial \overline{u}}{\partial y} + \frac{\partial \overline{v}}{\partial x}\right) + v'v'\frac{\partial \overline{v}}{\partial y}\right). \tag{9}$$

Clearly, a positive BT indicates that EKE is being transferred from the mean flow to the eddy fluctuations.

It's known that specific physical problems may involve different definitions of mean flow or eddy fluctuations. Nevertheless, the BT can still function as an indicator of barotropic instability (Fujii et al., 2008). In the context of the specific issue at hand, the predicted reference state, confined to the regions within rectangles that encompass both the initial and final locations of individual eddies, is regarded as the mean flow. The CNOPs and their evolutions are perceived as eddy fluctuations. Then, using the reference state from T_0 to T_1 obtained with the $k_b = 5$ setting in the QG model, we calculated the BT of the β-CNOP (CNOP calculated with the $k_b = 5$ setting as shown in Figure 1f) and f-CNOP (CNOP calculated with the $k_b = 0$ setting as shown in Figure 1b) over the optimization time by applying Equation 9, respectively.

It is found that, during the optimization time from T_0 to T_1, positive BT emerges in areas characterized by significant CNOPs and their evolutions, regardless of whether it is related to β-CNOP or f-CNOP, as depicted in Figure 5. Furthermore, at the initial time, the positive BT induced by the f-CNOP appears to be larger than that induced by the β-CNOP. However, during the optimization period, the positive BT induced by the β-CNOP undergoes greater development than that induced by the f-CNOP. As time progresses beyond the initial phase, the positive BT generated by the evolution of the β-CNOP becomes increasingly evident compared to that driven by the evolution of the f-CNOP, particularly during the mid to later stages of the optimization time. Notably, the superiority of the positive BT triggered by the β-CNOP compared to the f-CNOPin the mid to later stages significantly surpasses the advantage of the positive BT triggered by the f-CNOP compared to the β-CNOP at the initial time. This implies that, under the $k_b = 5$ condition of the model, more energy can be transferred from the

19422466, 2026, 8, Downloaded from https://agupubs.onlinelibrary.wiley.com/doi/10.1029/2026MS005831 by CochraneChina, Wiley Online Library on [31/07/2026]. See the Terms and Conditions (https://onlinelibrary.wiley.com/terms-and-conditions) on Wiley Online Library for rules of use; OA articles are governed by the applicable Creative Commons License

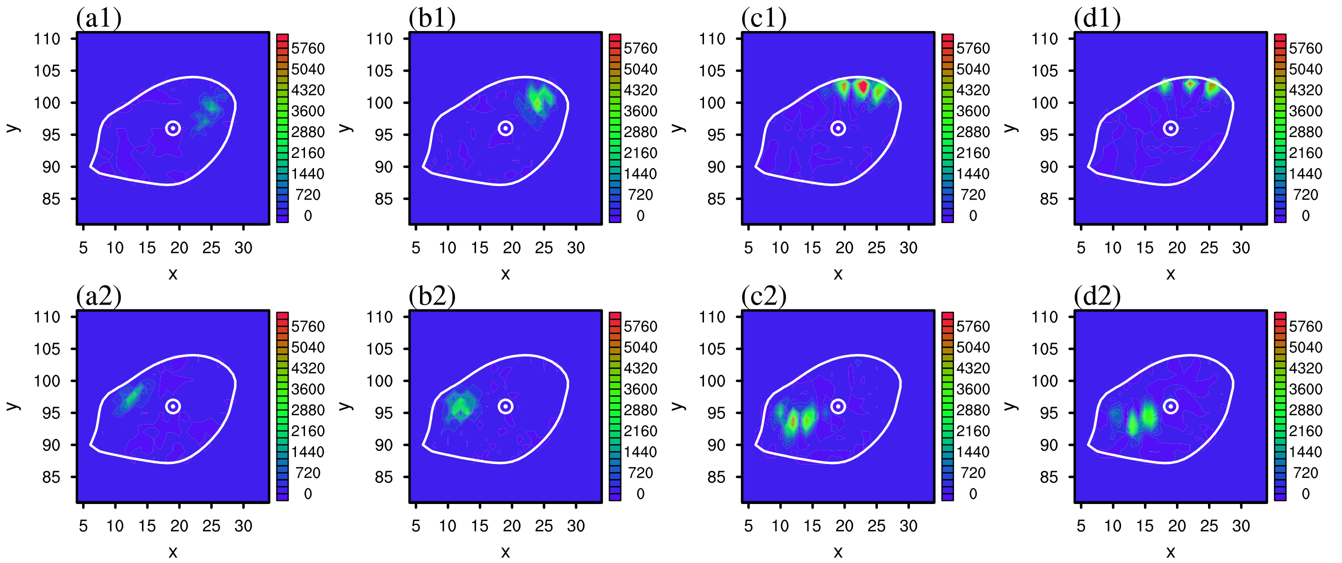

Figure 5. The evolution of the BT within the optimization time $[T_0,\ T_1]$ for the eddy shown in Figure 1a. Panels (a–d) correspond to the time T_0, (1/3) $(T_1 - T_0)$, (2/3) $(T_1 - T_0)$, and T_1, respectively. (1, 2) correspond to the BT resulting from β-CNOP and f-CNOP, respectively. The white contours delineate the edge of the initial eddy.

mesoscale eddies to β-CNOP type errors than to f-CNOP type errors throughout the entire optimization period. It's noteworthy that, besides their locations, both β-CNOP and f-CNOP exhibit identical structural characteristics, specifically a shear structure of the SSHA. That is, when this eddy is located at low latitudes, during the optimization time, initial errors manifesting a shear structure in the β-sensitive area, rather than the f-sensitive area, are more prone to extracting energy from the eddy due to barotropic instability and undergo substantial growth. This, in turn, has a crucial impact on the prediction of SSHA. In fact, the shear structure of CNOP-type errors has been interpreted in Jiang et al. (2022), which is more conducive to generating a large positive BT. Therefore, we need to pay more attention to the positional characteristics of the β-sensitive area and the f-sensitive area to understand the reasons for the aforementioned differences in BT induced by β-CNOP and f-CNOP.

Analyzing the positional characteristics of the β-sensitive area and the f-sensitive area, we find that they are closely related to the velocity fields, no matter the high-to low-velocity gradient in the β-and f-sensitive area or the eastward velocity component within the β-sensitive area. Hence, we visualized the velocity fields of the reference state obtained under the specified $k_b = 5$ setting in the QG model throughout the optimization period, which was used in Section 3 to calculate the CNOPs that identify the β-sensitive area. As shown in Figures 6a1–6d1, a notable reduction in the high-to low-velocity gradient within the f-sensitive area is observed over the optimization period. In contrast, the high-to low-velocity gradient in the β-sensitive area gradually becomes more pronounced and surpasses that in the f-sensitive area. This contrast is particularly evident when compared with the $k_b = 0$ condition shown in Figures 6a2–6d2. Referring to the equation $\mathrm{BT} = -\frac{V'^2}{(\overline{V}+V')} \cdot \frac{\partial \overline{V}}{\partial t}$ derived in a natural coordinate system in Jiang et al. (2022), the high-to low-velocity gradient along the eddy rotation ($\frac{\partial \overline{V}}{\partial t} < 0$) stimulates a positive BT between the reference state and initial errors. $\overline{V}$ represents the velocity of the mean flow (which serves as the reference state for prediction), while V' denotes the velocity of the eddy fluctuation field (corresponding to the CNOPs and their subsequent evolution). Consequently, as time progresses, the initial errors within the β-sensitive area, combined with the increasing density of the high-to low-velocity gradient from T_0 to T_1, result in a larger positive BT compared to the f-sensitive area, where the velocity gradient becomes weaker.

Indeed, under the specified $k_b = 5$ setting in the QG model, the gradual densification of the high-to low-velocity gradient within the β-sensitive area can be attributed to the presence of an eastward velocity component ($u > 0$). The meridional derivative of the Coriolis parameter, $\beta = 2\Omega \cos\theta/a$, is more pronounced at lower latitudes, where Ω denotes the angular velocity of the Earth's rotation, θ signifies the latitude, and a is the radius of the Earth. In practice, mesoscale eddies at lower latitudes tend to exhibit a stronger westward movement, owing to the enhanced influence of the planetary β-effect (Chelton et al., 2007; Nof, 1981; S. Yang et al., 2020) (see Figure 7). In contrast, the eastward velocity component ($u > 0$) in β-sensitive area counteracts the westward movement of

19422466, 2026, 8, Downloaded from https://agupubs.onlinelibrary.wiley.com/doi/10.1029/2026MS005831 by CochraneChina, Wiley Online Library on [31/07/2026]. See the Terms and Conditions (https://onlinelibrary.wiley.com/terms-and-conditions) on Wiley Online Library for rules of use; OA articles are governed by the applicable Creative Commons License

10.1029/2026MS005831

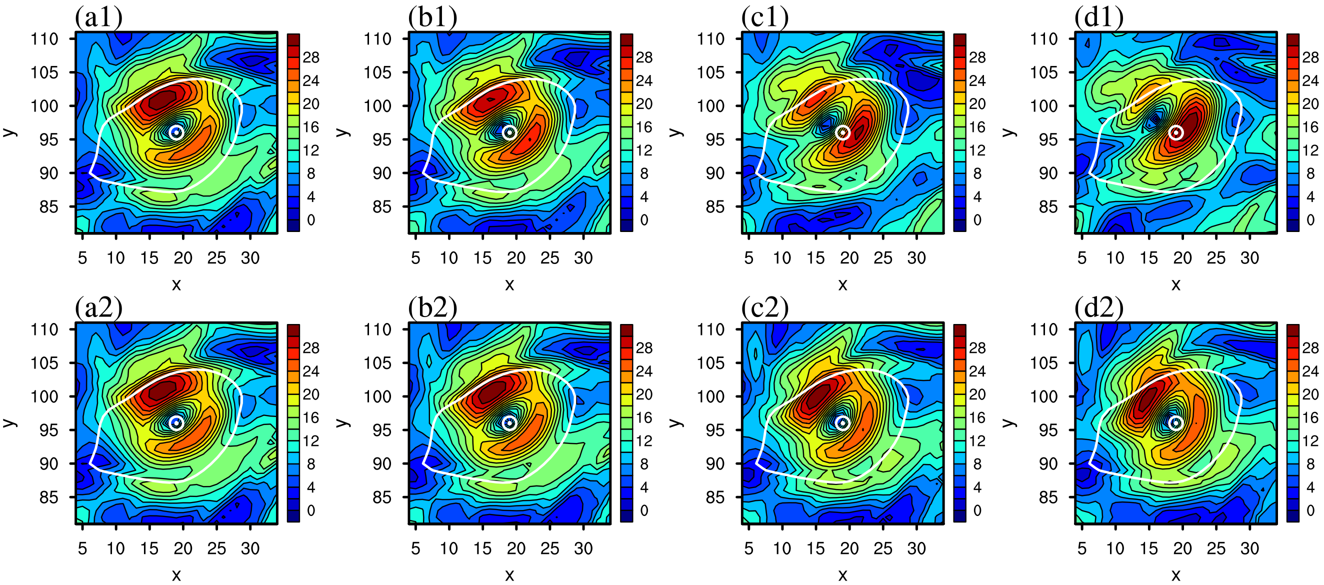

Figure 6. The evolution of the velocity (shaded) within the optimization time $[T_0, T_1]$ of the eddy shown in Figure 1a. (a, b, c, d) correspond to the time T_0, (1/3) $(T_1 - T_0)$, (2/3) $(T_1 - T_0)$, and T_1, respectively. (1, 2) correspond to the situation in the $k_b = 5$ and $k_b = 0$ settings of the QG model, respectively, and their comparison offers a clearer insight into the issue. The white contours delineate the edge of the initial eddy.

the vortex accelerated by the planetary β-effect. As a result, the opposition between the eastward velocity component and the westward movement intensifies at lower latitudes, leading to a greater accumulation of water mass in the β-sensitive area and a more pronounced high-to low-velocity gradient here. From this perspective, we can also explain why, in cases where the intensity difference between high-to low-velocity gradient regions within the eddy is particularly pronounced, the CNOPs consistently concentrate within the strongest gradient region, regardless of the value of k_b in the QG model, as discussed in Section 3. This occurs because, in such cases, even if an eastward velocity component exists in the weaker gradient region, the encrypted velocity gradient caused by it during the optimization period is still less pronounced than the gradient in the strongest gradient region. As a

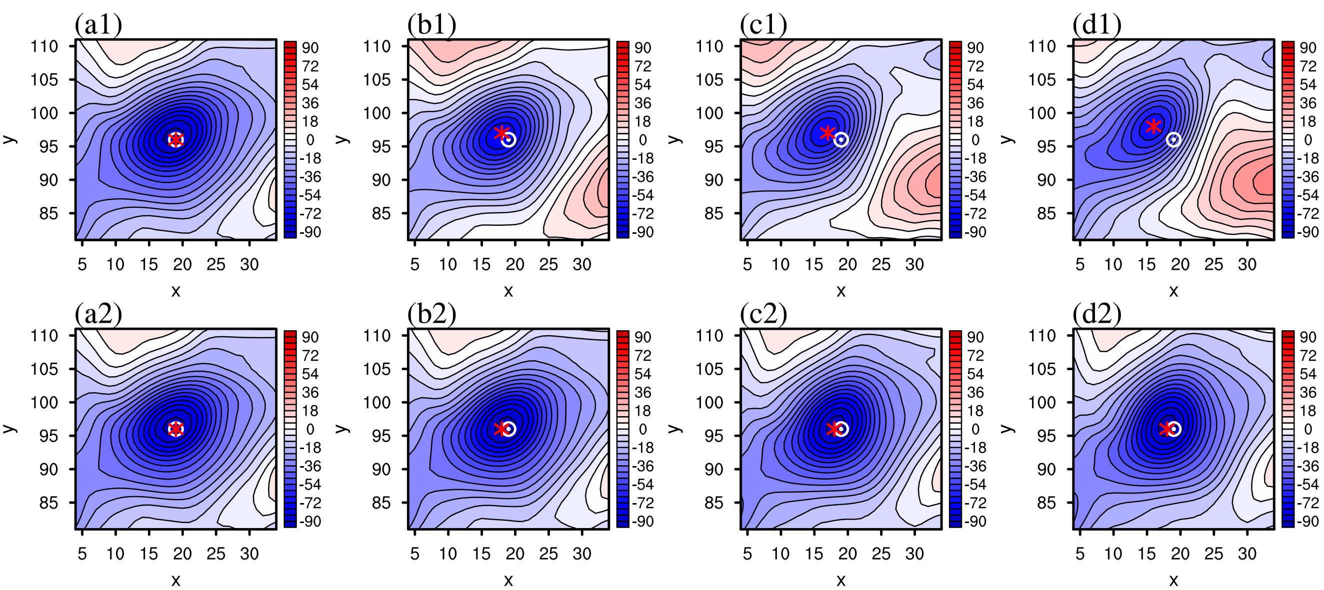

Figure 7. The evolution of the sea surface height anomaly (shaded) within the optimization time $[T_0, T_1]$ of the eddy shown in Figure 1a. Panels (a–d) correspond to the time T_0, (1/3) $(T_1 - T_0)$, (2/3) $(T_1 - T_0)$, and T_1, respectively. (1, 2) correspond to the situation in the $k_b = 5$ and $k_b = 0$ settings of the QG model, respectively, and their comparison offers a clearer insight into the issue.

19422466, 2026, 8, Downloaded from https://agupubs.onlinelibrary.wiley.com/doi/10.1029/2026MS005831 by CochraneChina, Wiley Online Library on [31/07/2026]. See the Terms and Conditions (https://onlinelibrary.wiley.com/terms-and-conditions) on Wiley Online Library for rules of use; OA articles are governed by the applicable Creative Commons License

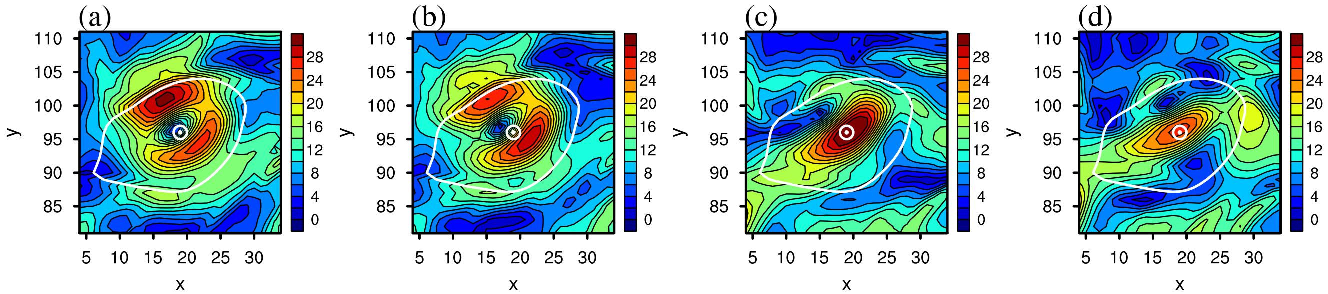

Figure 8. The evolution of the velocity (shaded) within the optimization time $[T_0, T_1]$ of the eddy shown in Figure 1a, corresponding to the situation in the $k_b = 10$ setting of the QG model. Panels (a–d) correspond to the time T_0, (1/3) $(T_1 - T_0)$, (2/3) $(T_1 - T_0)$, and T_1, respectively. The white contours delineate the edge of the initial eddy.

result, the positive BT in the weaker gradient region is smaller than in the strongest gradient region, and the eastward velocity no longer serves as a determining factor in identifying the most sensitive area.

Additionally, from the OSSEs in Section 4, we note that the benefit of assimilation in the β-sensitive area under the specified $k_b = 10$ setting is less than that under the specified $k_b = 5$ setting (see Figure 4). This can be attributed to the faster westward movement of the vortex driven by the stronger β-effect under the $k_b = 10$ setting, which corresponds to a lower latitude than the situation within the $k_b = 5$ setting. In this case, the eastward velocity component ($u > 0$) in the β-sensitive area is insufficient to counteract the stronger westward tendency of the vortex induced by the stronger β-effect toward the end of the optimization period (see Figure 8). As a result, the accumulated high-to low-velocity gradient structure in the β-sensitive area, which is beneficial for generating large positive BT, is partially disrupted, particularly toward the later stages of the optimization period. Consequently, the development of initial errors in the β-sensitive area is less pronounced in this situation within the $k_b = 10$ setting, and the preferential assimilation of observations in the β-sensitive area is less effective than under the specified $k_b = 5$ setting in the model. Nevertheless, this does not negate the fact that the β-sensitive area remains significantly more effective than the f-sensitive area in this context, as shown in Figure 4.

6. Summary and Discussion

In the present study, we investigate the sensitive areas for targeted observations of mesoscale eddies relevant to SSHA forecasting and reveal their pronounced latitude dependence. Using the CNOP approach, the most sensitive initial perturbations relevant to SSHA forecasting were first calculated for mesoscale eddies under different values of the parameter k_b in a two-layer QG model, representing different latitudinal settings. The resulting CNOPs sometimes exhibit variations in their spatial characteristics across different k_b regimes. Based on the high-value regions of the CNOPs, which indicate strong sensitivity to initial errors in SSHA forecasts, the sensitive areas of mesoscale eddies were identified. The results show that the location characteristics of sensitive areas may vary with latitude. For eddies in high-latitude bands (latitude > 60°), the sensitive areas are typically located where the high-to low-velocity gradients within the mesoscale eddies are most pronounced. However, for eddies in low-latitude bands (latitude < 30°), the sensitive areas tend to occur in regions where (relatively weaker) high-to low-velocity gradient coexist with an eastward zonal flow. In other words, for low-latitude eddies, in addition to the magnitude of the high-to low-velocity gradients, the direction of the zonal velocity within the gradient region also plays an important—though not decisive - role in determining the sensitive areas for SSHA forecasting. For eddies in mid-latitude bands (30° < latitude < 60°), both types of sensitive areas may contribute significantly to improving SSHA forecasts.

Subsequently, OSSEs were conducted to evaluate the effectiveness of the sensitive areas identified for mesoscale eddies at different latitudes. The results demonstrate that prioritizing data assimilation within these latitude-dependent sensitive areas significantly improves the skill of SSHA forecasts. In particular, this study highlights the effectiveness of sensitive areas characterized by relatively weaker high-to low-velocity gradient coexisting with an eastward zonal velocity component, especially for eddies located in mid- and low-latitude bands, which has not been identified in previous studies. These results provide valuable insights into the optimal allocation of target observations for mesoscale eddies, emphasizing the importance of considering the

19422466, 2026, 8, Downloaded from https://agupubs.onlinelibrary.wiley.com/doi/10.1029/2026MS005831 by CochraneChina, Wiley Online Library on [31/07/2026]. See the Terms and Conditions (https://onlinelibrary.wiley.com/terms-and-conditions) on Wiley Online Library for rules of use; OA articles are governed by the applicable Creative Commons License

latitude of mesoscale eddies when designing observation or assimilation strategies, ultimately contributing to more efficient improvements in SSHA forecasting.

Finally, from a dynamical perspective, the latitude dependence of sensitive areas in mesoscale eddies can be physically interpreted in terms of barotropic instability associated with the planetary β-effect. Mesoscale eddies at different latitudes are influenced by the β-effect to varying degrees. Accordingly, for eddies at high latitudes, which are less affected by the planetary β-effect, regions exhibiting the strongest high-to low-velocity gradients within the initial eddies sustain the largest barotropic energy conversion rates, leading to the fastest growth of initial errors and thus playing a dominant role in SSHA forecasting. In contrast, at low latitudes, regions within the initial eddies that contain (relatively weaker) high-to low-velocity gradients coexisting with an eastward zonal velocity component are more likely to generate larger barotropic energy conversion rates during the optimization period due to local water accumulation influenced by the planetary β-effect, thereby promoting error growth through barotropic instability. Consequently, for low-latitude eddies, prioritizing the assimilation of observations within sensitive areas characterized by (relatively weaker) high-to low-velocity gradients coexisting with an eastward zonal flow is likely to be more effective.

It is worth noting that, to facilitate comparison with previous studies, the present work is confined to a two-layer QG framework, with particular emphasis on surface flow. The effectiveness and robustness of the latitude-dependent sensitive areas require further validation with real ocean data under realistic conditions in future work. In addition, real ocean dynamics involve substantially greater complexity than that represented in the present model. Mesoscale eddies often possess three-dimensional structures, and subsurface mesoscale eddies have also been observed. In such a context, sensitive areas may be further influenced by dynamical processes such as baroclinic instability, submesoscale motions, and wind forcing, as well as broader background environmental variability (Ding et al., 2023; Liao et al., 2019; Tian et al., 2025; X. Wang et al., 2022; Zhong et al., 2026). A more holistic consideration of these processes is expected to yield a more comprehensive understanding of the sensitive areas associated with mesoscale eddies, with implications not only for SSHA forecasting but also for other oceanic variables, and offering valuable guidance for internal observations, such as Argo buoy deployments. It should be noted that solving CNOPs for complex realistic models remains computationally expensive. In the present study, a single CNOP computation typically requires several days, and the cost may increase substantially with higher model dimensionality and complexity. For practical applications, more efficient algorithms are therefore required, particularly for gradient computation and CNOP estimation. In this regard, several realistic models already possess well-developed adjoint systems that can be directly used for this purpose, such as the Regional Ocean Modeling System. In addition, a variety of intelligent optimization algorithms, such as particle swarm optimization and genetic algorithms, have been developed to tackle high-dimensional optimization problems. Since these methods do not explicitly require gradient information, they provide alternative approaches for CNOP computations across models of varying complexity. Furthermore, artificial intelligence is currently developing rapidly. AI-based weather forecasting models have emerged internationally, such as FuXi and PanGu, which have demonstrated strong capability in forecasting high-impact weather events. Li et al. (2025) showed that integrating the CNOP method into the FuXi model can significantly improve tropical cyclone track forecasts, with CNOPs directly computed using the automatic differentiation algorithm embedded in the FuXi model. If AI models capable of adequately representing mesoscale ocean eddy evolution are developed, CNOP methods could be further incorporated into such frameworks to enable more efficient identification of eddy-sensitive areas. Ultimately, CNOP analysis is expected to become increasingly applicable to realistic ocean prediction systems. The overarching goal is to design an optimal observation network for mesoscale eddies and substantially enhance the accuracy of ocean state forecasts.

Conflict of Interest

The authors declare no conflicts of interest relevant to this study.

Availability Statement

All scripts employed for data analysis and figure generation were developed using NCL (https://www.ncl.ucar.edu) and MATLAB (https://www.mathworks.com/products/matlab.html). The scripts and data sets generated

19422466, 2026, 8, Downloaded from https://agupubs.onlinelibrary.wiley.com/doi/10.1029/2026MS005831 by CochraneChina, Wiley Online Library on [31/07/2026]. See the Terms and Conditions (https://onlinelibrary.wiley.com/terms-and-conditions) on Wiley Online Library for rules of use; OA articles are governed by the applicable Creative Commons License

and/or analyzed during the study, together with the configurations of the QG code, can be accessed in Jiang et al. (2026) at https://doi.org/10.5281/zenodo.18468805.

Acknowledgments

The authors are very grateful for the constructive suggestions provided by the editor, Prof. Ian Grooms, during the first submission, which played an important role in improving the reliability of the numerical results and the overall significance of the study. The authors also thank the three anonymous reviewers for their valuable comments and helpful suggestions. This study was jointly supported by the National Natural Science Foundation of China (Grants 42406007; 42330111) and the Natural Science Foundation of Shandong Province of China (Grant ZR2023QD158). We also acknowledge the technical support of the National Large Scientific and Technological Infrastructure “Earth System Numerical Simulation Facility” (https://cstr.cn/31134.02.EL).

References

Birgin, E. G., Martínez, J., & Raydan, M. (1999). Nonmonotone spectral projected gradient methods on convex sets. *SIAM Journal on Optimization*, *10*(4), 1196–1211. https://doi.org/10.1137/S1052623497330963

Chan, P., Han, W., Mak, B., Qin, X., Liu, Y., Yin, R., & Wang, J. (2023). Ground-space-sky observing system experiment during tropical cyclone Mulan in August. *Advances in Atmospheric Sciences*, *40*(2), 194–200. https://doi.org/10.1007/s00376-022-2267-z

Chelton, D. B. (2013). Mesoscale eddy effects. *Nature Geoscience*, *6*(8), 594–595. https://doi.org/10.1038/ngeo1906

Chelton, D. B., Schlax, M. G., & Samelson, R. M. (2011). Global observations of nonlinear mesoscale eddies. *Progress in Oceanography*, *91*(2), 167–216. https://doi.org/10.1016/j.pocean.2011.01.002

Chelton, D. B., Schlax, M. G., Samelson, R. M., & de Szoeke, R. A. (2007). Global observations of large oceanic eddies. *Geophysical Research Letters*, *34*(15), L15606. https://doi.org/10.1029/2007GL030812

Cotton, P. D., & Menard, Y. (2006). Future requirements for satellite altimetry: Recommendations from the EC GAMBLE project. In *15 Years of Progress in Radar Altimetry Symposium, Venice, Italy* (pp. 13–18). ESA.

Ding, R., Nnamchi, H. C., Yu, J. Y., Li, T., Sun, C., Li, J., et al. (2023). North Atlantic oscillation controls multidecadal changes in the North Tropical Atlantic Pacific connection. *Nature Communications*, *14*(1), 862. https://doi.org/10.1038/s41467-023-36564-3

Dong, C., McWilliams, J. C., Liu, Y., & Chen, D. (2014). Global heat and salt transports by eddy movement. *Nature Communications*, *5*(1), 3294. https://doi.org/10.1038/ncomms4294

Duan, W., Li, X., & Tian, B. (2018). Towards optimal observational array for dealing with challenges of El Niño-Southern Oscillation predictions due to diversities of El Niño. *Climate Dynamics*, *51*(9–10), 3351–3368. https://doi.org/10.1007/s00382-018-4082-x

Feng, J., Wang, J., Dai, G. K., Zhou, F. F., & Duan, W. S. (2023). Spatiotemporal estimation of analysis errors in the operational global data assimilation system at the China Meteorological Administration using a modified SAFE method. *Quarterly Journal of the Royal Meteorological Society*, *149*(755), 2301–2319. https://doi.org/10.1002/qj.4507

Feng, R., & Duan, W. (2025). Sensitive area in the tropical Indian Ocean for advancing beyond the summer predictability barrier of Indian Ocean Dipole. *Dynamics of Atmospheres and Oceans*, *110*, 101552. https://doi.org/10.1016/j.dynatmoce.2025.101552

Frenger, I., Gruber, N., Knutti, R., & Munnich, M. (2013). Imprint of Southern Ocean eddies on winds, clouds and rainfall. *Nature Geoscience*, *6*(8), 608–612. https://doi.org/10.1038/ngeo1863

Fujii, Y., Tsujino, H., Usui, N., Nakano, H., & Kamachi, M. (2008). Application of singular vector analysis to the Kuroshio large meander. *Journal of Geophysical Research*, *113*(C7), C0702. https://doi.org/10.1029/2007JC004476

Gelaro, R., Langland, R. H., Pellerin, S., & Todling, R. (2010). The THORPEX observation impact intercomparison experiment. *Monthly Weather Review*, *138*(11), 4009–4025. https://doi.org/10.1175/2010MWR3393.1

Hoffman, R., & Atlas, R. (2016). Future observing system simulation experiments. *Bulletin of the American Meteorological Society*, *97*(9), 1601–1616. https://doi.org/10.1175/BAMS-D-15-00200.1

Janjic, T., Bormann, N., Bocquet, M., Carton, J. A., Cohn, S. E., Dance, S. L., et al. (2018). On the representation error in data assimilation. *Quarterly Journal of the Royal Meteorological Society*, *144*(713), 1257–1278. https://doi.org/10.1002/qj.3130

Jiang, L., Duan, W., & Liu, H. (2022). The most sensitive initial error of sea surface height anomaly forecasts and its implication for target observations of mesoscale eddies. *Journal of Physical Oceanography*, *52*(4), 723–740. https://doi.org/10.1175/JPO-D-21-0200.1

Jiang, L., Duan, W., & Wang, H. (2024). The sensitive area for targeting observations of paired mesoscale eddies associated with sea surface height anomaly forecasts. *Journal of Geophysical Research: Oceans*, *129*(2), e2023JC020572. https://doi.org/10.1029/2023JC020572

Jiang, L., Duan, W., & Wang, H. (2026). Latitude-dependent sensitive areas for targeted observations of mesoscale eddies associated with sea surface height anomaly forecasts [Dataset]. *Zenodo*. https://doi.org/10.5281/zenodo.18468805

Jiang, L., Duan, W., Wang, H., Liu, H., & Tao, L. (2023). Evaluation of the sensitivity on mesoscale eddy associated with the sea surface height anomaly forecasting in the Kuroshio Extension. *Frontiers in Marine Science*, *10*, 1097209. https://doi.org/10.3389/fmars.2023.1097209

Kramer, W., Dijkstra, H. A., Pierini, S., & van Leeuwen, P. J. (2012). Measuring the impact of observations on the predictability of the Kuroshio Extension in a shallow-water model. *Journal of Geophysical Research*, *42*(1), 3–17. https://doi.org/10.1175/JPO-D-11-014.1

Li, Y., Duan, W., Han, W., Li, H., & Qin, X. (2025). Improving tropical cyclone track forecast skill through assimilating target observation achieved by AI-based conditional nonlinear optimal perturbation. *Journal of Geophysical Research: Atmospheres*, *130*(9), e2024JD043261. https://doi.org/10.1029/2024JD043261

Li, Y., Peng, S., & Liu, D. (2014). Adaptive observation in the South China Sea using CNOP approach based on a 3-D ocean circulation model and its adjoint model. *Journal of Geophysical Research: Oceans*, *119*(12), 8973–8986. https://doi.org/10.1002/2014JC010220

Liang, P., Mu, M., Wang, Q., & Yang, L. (2019). Optimal precursors triggering the Kuroshio intrusion into the South China Sea obtained by the conditional nonlinear optimal perturbation approach. *Journal of Geophysical Research: Oceans*, *124*(6), 3941–3962. https://doi.org/10.1029/2018JC014545

Liao, G., Xu, X., Dong, C., Cao, H., & Wang, T. (2019). Three-dimensional baroclinic eddies in the ocean: Evolution, propagation, overall structures, and angular models. *Journal of Physical Oceanography*, *49*(10), 2571–2599. https://doi.org/10.1175/JPO-D-18-0237.1

Liu, K., Guo, W., Da, L., Liu, J., Hu, H., & Cui, B. (2021). Improving the thermal structure predictions in the Yellow Sea by conducting targeted observations in the CNOP-identified sensitive areas. *Scientific Reports*, *11*(1), 19518. https://doi.org/10.1038/s41598-021-98994-7

Mu, M. (2013). Methods, current status, and prospect of targeted observation. *Science China Earth Sciences*, *56*(12), 1997–2005. https://doi.org/10.1007/s11430-013-4727-x

Mu, M., Duan, W., & Wang, B. (2003). Conditional nonlinear optimal perturbation and its applications. *Nonlinear Processes in Geophysics*, *10*(6), 493–501. https://doi.org/10.5194/npg-10-493-2003

Mu, M., Zhou, F., & Wang, H. (2009). A method for identifying the sensitive areas in targeted observations for tropical cyclone prediction: Conditional nonlinear optimal perturbation. *Monthly Weather Review*, *137*(5), 1623–1639. https://doi.org/10.1175/2008MWR2640.1

Ni, Q., Zhai, X., Wang, G., & Hughes, C. W. (2020). Widespread mesoscale dipoles in the global ocean. *Journal of Geophysical Research: Oceans*, *125*(10), e2020JC016479. https://doi.org/10.1029/2020jc016479

Nof, D. (1981). On the β-induced movement of isolated baroclinic eddies. *Journal of Physical Oceanography*, *11*(12), 1662–1672. https://doi.org/10.1175/1520-0485(1981)011<1662:otimoi>2.0.co;2

19422466, 2026, 8, Downloaded from https://agupubs.onlinelibrary.wiley.com/doi/10.1029/2026MS005831 by CochraneChina, Wiley Online Library on [31/07/2026]. See the Terms and Conditions (https://onlinelibrary.wiley.com/terms-and-conditions) on Wiley Online Library for rules of use; OA articles are governed by the applicable Creative Commons License

Qin, X., Duan, W., Chan, P., Chen, B., & Huang, K. (2022). Effects of dropsonde data in field campaigns on forecasts of tropical cyclones over the western North Pacific in 2020 and role of CNOP sensitivity. *Advances in Atmospheric Sciences*, *40*(5), 791–803. https://doi.org/10.1007/s00376-022-2136-9

Robinson, A. R. (1983). *Eddies in marine science* (p. 612). Springer.

Snyder, C. (1996). Summary of an informal workshop on adaptive observations and FASTEX. *Bulletin of the American Meteorological Society*, *77*(5), 953–961. https://doi.org/10.1175/1520-0477-77.5.953

Tang, Q., Gulick, S. P. S., Sun, J., Sun, L., & Jing, Z. (2020). Submesoscale features and turbulent mixing of an oblique anticyclonic eddy in the Gulf of Alaska investigated by marine seismic survey data. *Journal of Geophysical Research: Oceans*, *125*(1), e2019JC015393. https://doi.org/10.1029/2019jc015393

Tian, Q., Yu, J.-Y., Nnamchi, H. C., Li, T., Li, J., Li, X., & Ding, R. (2025). Unraveling the mystery of recent shortened response time of ENSO to Atlantic forcing. *Nature Communications*, *16*(1), 5884. https://doi.org/10.1038/s41467-025-61130-4

Tsujino, H., Usui, N., & Nakano, H. (2006). Dynamics of Kuroshio path variations in a high-resolution general circulation model. *Journal of Geophysical Research*, *111*(C11), C11001. https://doi.org/10.1029/2005JC003118

Wang, Q., Mu, M., & Dijkstra, H. A. (2013). Effects of nonlinear physical processes on optimal error growth in predictability experiments of the Kuroshio Large Meander. *Journal of Geophysical Research: Oceans*, *118*(12), 6425–6436. https://doi.org/10.1002/2013JC009276

Wang, X., Du, Y., Zhang, Y., Wang, T., Wang, M., & Jing, Z. (2022). Subsurface anticyclonic eddy transited from Kuroshio shedding eddy in the northern South China Sea. *Journal of Physical Oceanography*, *53*(3), 841–861. https://doi.org/10.1175/JPO-D-22-0106.1

Weiss, J. B., & Grooms, I. (2017). Assimilation of ocean sea-surface height observations of mesoscale eddies. *Chaos*, *27*(12), 126803. https://doi.org/10.1063/1.4986088

Wu, C. C., Chen, J. H., Lin, P. H., & Chou, K. H. (2007). Targeted observations of tropical cyclone movement based on the adjoint-derived sensitivity steering vector. *Journal of the Atmospheric Sciences*, *64*(7), 2611–2626. https://doi.org/10.1175/JAS3974.1

Wu, C. C., Chen, J. H., Majumdar, S. J., Peng, M. S., Reynolds, C. A., Aberson, S. D., et al. (2009). Inter-comparison of targeted observation guidance for tropical cyclones in the northwestern Pacific. *Monthly Weather Review*, *137*(8), 2471–2492. https://doi.org/10.1175/2009MWR2762.1

Wunsch, C. (1999). Where do ocean eddy heat fluxes matter? *Journal of Geophysical Research*, *104*(C6), 13235–13249. https://doi.org/10.1029/1999jc900062

Yang, L., & Duan, W. (2024). Sensitive areas for target observation associated with meteorological forecasts for dust storm events in the Beijing-Tianjin-Hebei region. *Quarterly Journal of the Royal Meteorological Society*, *151*(770), e4975. https://doi.org/10.1002/qj.4975

Yang, L., Duan, W., & Wang, Z. (2023). An approach to refining the ground meteorological observation stations for improving $PM_{2.5}$ forecasts in the Beijing-Tianjin-Hebei region. *Geoscientific Model Development*, *16*(13), 3827–3848. https://doi.org/10.5194/gmd-16-3827-2023

Yang, L., Duan, W., Wang, Z., & Yang, W. (2022). Toward targeted observations of the meteorological initial state for improving the $PM_{2.5}$ forecast of a heavy haze event that occurred in the Beijing-Tianjin-Hebei region. *Atmospheric Chemistry and Physics*, *22*(17), 11429–11453. https://doi.org/10.5194/acp-22-11429-2022

Yang, S., Xing, J., Sheng, J., Chen, S., Tian, J., & Chen, D. (2020). The impact of the planetary β-effect on the vertical structure of a coherent vortex in the South China Sea. *Ocean Dynamics*, *70*(7), 879–896. https://doi.org/10.1007/s10236-020-01375-3

Zhang, K., Mu, M., Wang, Q., Yin, B., & Liu, S. (2019). CNOP-based adaptive observation network designed for improving upstream Kuroshio transport prediction. *Journal of Geophysical Research: Oceans*, *124*(6), 4350–4364. https://doi.org/10.1029/2018JC014490

Zhang, Y., Chen, X., & Dong, C. (2019). Anatomy of a cyclonic eddy in the Kuroshio Extension based on high-resolution observations. *Atmosphere*, *10*(9), 553. https://doi.org/10.3390/atmos10090553

Zhang, Z., Wang, W., & Qiu, B. (2014). Oceanic mass transport by mesoscale eddies. *Science*, *345*(6194), 322–324. https://doi.org/10.1126/science.1252418

Zhong, Q., Chan, J. C. L., Duan, W., Tu, S., Li, J., Gan, J., & Ding, R. (2026). Landfalling tropical cyclones accelerate due to land-sea thermal and roughness contrasts. *Nature Geoscience*, *19*(2), 159–164. https://doi.org/10.1038/s41561-025-01891-1

19422466, 2026, 8, Downloaded from https://agupubs.onlinelibrary.wiley.com/doi/10.1029/2026MS005831 by CochraneChina, Wiley Online Library on [31/07/2026]. See the Terms and Conditions (https://onlinelibrary.wiley.com/terms-and-conditions) on Wiley Online Library for rules of use; OA articles are governed by the applicable Creative Commons License